General Disclaimer

One or more of the Following Statements may affect this Document
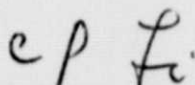
- This document has been reproduced from the best copy furnished by the organizational source. It is being released in the interest of making available as much information as possible.

- This document may contain data, which exceeds the sheet parameters. It was furnished in this condition by the organizational source and is the best copy available.

- This document may contain tone-on-tone or color graphs, charts and/or pictures, which have been reproduced in black and white.

- This document is paginated as submitted by the original source.

- Portions of this document are not fully legible due to the historical nature of some of the material. However, it is the best reproduction available from the original submission.
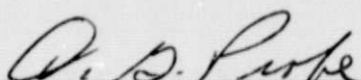
Produced by the NASA Center for Aerospace Information (CASI)

TECHNICAL REPORT

COMPUTATIONS OF SUPERSONIC VISCOUS FLOW OVER

A FINITE-WIDTH PLATE

Job Order 81-067

Prepared by

Lockheed Electronics Company, Inc.

Systems and Services Division

Houston, Texas

for

STRUCTURES AND MECHANICS DIVISION

National Aeronautics and Space Administration

LYNDON B. JOHNSON SPACE CENTER

Houston, Texas

August 1977

LEC-10644

TECHNICAL REPORT

COMPUTATIONS OF SUPERSONIC VISCOUS FLOW OVER
A FINITE-WIDTH PLATE

Job Order 81-067

PREPARED BY

_C. P. Li_

APPROVED BY

D. G. Probe, Supervisor
Structures Technology Section

W. J. Reicks, Manager
Applied Mechanics Department

Prepared By

Lockheed Electronics Company, Inc.

For

Structures and Mechanics Division

NATIONAL AERONAUTICS AND SPACE ADMINISTRATION
LYNDON B. JOHNSON SPACE CENTER
HOUSTON, TEXAS

August 1977

FOREWORD

This report discusses the numerical solutions obtained for the simplest three-dimensional configuration, a flat plate, using the simplified Navier-Stokes equations. A separate report is being written to present the results for an axial corner formed by two perpendicular plates. The leading-edge problem, which is essentially two-dimensional, has been studied using both the exact and the simplified Navier-Stokes equations, and will be described in another report. These program listings and user's guide are to be documented in the fourth report.

CONTENTS

COMPUTATIONS OF SUPERSONIC VISCOUS FLOW OVER
A FINITE-WIDTH PLATE

ABSTRACT

Finite-difference methods are applied to solve the parabolic Navier-Stokes equations for the flow over a finite-width plate at 0° and 10° angles of attack. The methods are developed on the basis of the operator-factorization concept resulting in the split of a three-dimensional equation into successive two-dimensional equations. Two versions of the factorization, backward and centered implicit schemes, are used and their results are compared. Available numerical solutions and experimental data obtained at low Reynolds number conditions are also used for comparison. The backward implicit method provides a more successful solution, which ranges from the merged-layer to the strong-interaction regimes. The present study also reveals the detailed structures of the shear layer around and behind the side edge.

1. INTRODUCTION

The problem of calculating viscous flow over simple configurations has been of practical importance in fluid dynamics in connection, for example, with the design of high-speed flying vehicles and with the investigation of flow phenomena in test facilities. It is known that the viscous and heat conducting effects not only dominate the flow within a narrow layer adjacent to the solid boundary, but also play an important role in shaping the flow structures near the leading edge, around the side edge, and behind the object. These flow fields, being far more complex and interesting than their two-dimensional counterparts, are not amenable to most of the existing methods of analysis due to some basic difficulties. In the first place, the governing equations, known as the Navier-Stokes equations, although providing an excellent description of the flow field, are an elliptic type for which the numerical techniques are lengthy and cumbersome. Secondly, because of the occurrence of shocks and shear layers resulting in steep gradients of flow properties, sufficiently fine resolution is required to maintain acceptable accuracy as well as a stable solution. Thus, even in some situations in which numerical solution is feasible, the computation cost is prohibitively high for frequent applications. Consequently, there have been some attempts to solve the flow problems with slightly different governing equations which possess parabolicity in one of the independent variables, usually along the coordinate defining the main flow velocity. This set of equations, termed as the parabolic Navier-Stokes equations, is to be integrated spatially and requires simpler and efficient numerical techniques, compared to that for the elliptic Navier-Stokes equations. The object of the present work is to develop a new algorithm to solve the parabolic equations and to evaluate its validity using a problem of the flow passing a finite-width plate.

There exists strong evidence that the parabolic Navier-Stokes equations can be used successfully to describe a large class of flow problems in which the physical dissipations and the pressure gradient can be neglected in the direction of the main flow. For example, ref. 1 and 2 have presented solutions of the incompressible flow inside a rectangular duct, and ref. 3 and 4 have discussed their techniques for solving the compressible flow over

2

a cone, an axial corner, and a finite-width plate. Although the problem studied may be different in flow property and in geometry, the governing equations employed have a close resemblance in the underlying assumption that the streamwise second-order derivatives can be omitted from the complete Navier-Stokes equations. Furthermore, the numerical techniques developed are typified by finite-difference integrations marching from one plane to the next, both normal to the streamwise coordinate. The implicit schemes (ref. 1,2,4) are preferable over the explicit ones, owing to their unconditional stability which allows a larger increment in the marching direction regardless of the fact that steep gradients necessitate fine discretization of the space on the integration plane. The combination usage of iterative and implicit schemes (ref. 3) is particularly appealing when the second-order derivatives are only present in one direction. In this technique and the ADI technique (ref. 4), the solution of a sparse-banded linear system of equations resulting from the direct application of implicit schemes to the governing equation is replaced by the solution of a tridiagonal system. The advantages achieved in more efficient computation far outweighs the extra work involved. This also suggests a further exploitation of the method of splitting (ref. 5) to construct other versions of difference techniques that may have more desirable features in the stability, accuracy and in the efficiency for practical computations of three-dimensional flowfields. The essential concept of splitting is to seek the solution of a multidimensional equation in two or three steps, each involving the solution to a two-dimensional equation. In terms of difference operators, this idea can be worked out readily by means of factorization, similar to that for an algebraic equation.

The other part of the numerical algorithm involving the formulation of difference equations and the solution to the nonlinear equations also receive considerable attention in this study. A mesh of cells, instead of points, is used because of its recognized compatibility to satisfy the conservative laws, both locally and globally (ref. 6). The cell formulation is recommended for flow containing large gradients and for separated flows. In order to solve the nonlinear difference equations, an iterative procedure is developed which retains the conservative property after the convergence is reached. A pre-

scribed tolerance on the order of the truncation error in the difference scheme is used to control the linearization error. These aspects are as important as the difference schemes to the success of computation, and hence deserve equal attention in the development of a numerical algorithm.

As a test case for the new algorithm, the flow past a finite-width plate at 0° and 10° angles of attack is considered. This problem was solved in ref. 4 using an ADI technique and its solution was among one of the earlier successful applications of the parabolic Navier-Stokes equations. However, it appears from the published results that the computation was terminated prematurely at a station quite close to the leading edge and that the inviscid-viscous interactions near the side edge are not as strong as anticipated. These difficulties may be caused in part by the fact that the ADI scheme is only marginally stable and therefore not suited to deal with solutions containing rapid variations, and in part by the use of a uniform mesh system which would fail to detect any sharp change in properties around the side edge.

The following discussion is divided into five sections, each concentrating on one aspect of the numerical solution. They are given in the order of the finite-difference methods, nonlinear difference equations, governing equations and boundary conditions, mesh system and stability, and the flowfield results.

2. FINITE DIFFERENCE METHODS

Consider a model partial differential equation in the conservative-law form

$$F_x + G_y + H_z = 0 \qquad (2\text{-}1)$$

where F, G, and H are column vectors and also the function of a column vector V. x, y and z are the Cartesian coordinates.

If the backward implicit scheme is applied directly to eq. (2-1), the resulting difference equation is

$$F_{jk}^{i+1} = F_{jk}^{i} - \frac{\Delta x_i}{\Delta y_j}\left(G_{j+\frac{1}{2}k}^{i+1} - G_{j-\frac{1}{2}k}^{i+1}\right) - \frac{\Delta x_i}{\Delta z_k}\left(H_{jk+\frac{1}{2}}^{i+1} - H_{jk-\frac{1}{2}}^{i+1}\right) + O\left(\Delta x_i^2\right) \qquad (2\text{-}2)$$

Subscripts j and k denote the locations of the cell point, $j\pm\frac{1}{2}k$ and $jk\pm\frac{1}{2}$ denote the location of the cell line. Superscripts i and i+1 refer to the previous and present values. The computation space defined in the y-z plane is discretized to have a mesh of cells, each having variable Δy_j and Δz_k. The integration increment, Δx_i, is also determined prior to solving eq. (2-2). Due to the nonlinear form of eq. (2-2), a linearization procedure is adapted to render a linear system of equation in terms of V_{jk}. This system of equations has a sparse-banded coefficient matrix, and requires lengthy computation. In practice, an ADI or an iterative-implicit technique in which the solution of a tridiagonal coefficient matrix is employed. The other alternative technique is the method of fractional steps, whereby the solution to eq.(2-2) is obtained from two equations

$$F_{jk}^{\star} = F_{jk}^{i} - \frac{\Delta x_i}{\Delta y_j}\left(G_{j+\frac{1}{2}k}^{\star} - G_{j-\frac{1}{2}k}^{\star}\right) + O\left(\Delta x_i^2\right)$$

$$F_{jk}^{i+1} = F_{jk}^{\star} - \frac{\Delta x_i}{\Delta z_k}\left(H_{jk+\frac{1}{2}}^{i+1} - H_{jk-\frac{1}{2}}^{i+1}\right) + O\left(\Delta x_i^2\right) \qquad (2\text{-}3)$$

The two successive steps constitute a cycle of the calculation, which can be efficiently performed just as the ADI technique since k and j are fixed in the first and the second equation, respectively.

A simple analysis can be carried out to demonstrate the equivalence between eqs.(2-2) and (2-3) to the order of $(\Delta x_i)^2$. Assuming F=G=H=V, eq.(2-2) can be written in the operator notation such as

$$LV^{i+1} = V^i \tag{2-4}$$

and eq.(2-3) becomes

$$L_y V^\star = V^i \ , \ L_z V^{i+1} = V^\star \tag{2-5}$$

where

$$LV = -\alpha V_{j-\frac{1}{2}k} + \alpha V_{j+\frac{1}{2}k} - \beta V_{jk-\frac{1}{2}} + \beta V_{jk+\frac{1}{2}}$$

$$L_y V = -\alpha V_{j-\frac{1}{2}k} + V_{jk} + \alpha V_{j+\frac{1}{2}k}$$

$$L_z V = -\beta V_{jk-\frac{1}{2}} + V_{jk} + \beta V_{jk+\frac{1}{2}}$$

with $\quad \alpha = \Delta x_i / \Delta y_j$ and $\beta = \Delta x_i / \Delta z_k$

By substituting the second into the first equation of eq.(2-5), it leads to

$$L_y L_z V = L_z L_y V = LV + 0\left(\Delta x_i^2\right)$$

Second-order accurate schemes may be constructed in the same manner. For example, using the centered scheme, the difference equations are

$$F_{jk}^\star = F_{jk}^i - \frac{\Delta x_i}{2\Delta y_j} \left(G_{j+\frac{1}{2}k}^i - G_{j-\frac{1}{2}k}^i + G_{j+\frac{1}{2}k}^\star - G_{j-\frac{1}{2}k}^\star\right) + 0\left(\Delta x_i^3\right)$$

$$F_{jk}^{i+1} = F_j^\star - \frac{\Delta x_i}{2\Delta z_k} \left(H_{jk+\frac{1}{2}}^\star - H_{jk-\frac{1}{2}}^\star + H_{jk+\frac{1}{2}}^{i+1} - H_{jk-\frac{1}{2}}^{i+1}\right) + 0\left(\Delta x_i^3\right) \tag{2-6}$$

6

or, in the operator notation

$$L_y V^* = \overline{L}_y V^i \quad , \quad L_z V^{i+1} = \overline{L}_z V^* \tag{2-7}$$

where

$$\overline{L}_y V = -\frac{1}{2} L_y V$$

and

$$\overline{L}_z V = -\frac{1}{2} L_z V$$

Eq.(2-6) can be shown to be equivalent to the difference equation of eq.(2-1) using the centered scheme in one step. Eq.(2-6) is more accurate than eq.(2-3) for smooth values of V. However eq.(2-3) is preferable when V has discontinuities because the backward scheme provides numerical dissipation to smooth out unwanted small wave-length oscillations.

The validity of approximating a multidimensional difference operator by a sequence of two-dimensional operators has not received full theoretical justification if the operators are nonlinear. Nevertheless, this method has been used for solutions of various nonlinear problems and has also been used successfully in the numerical applications. Finally the nonlinear operators do not commute with each other in general, the following equations are used instead. Eqs.(2-3) and (2-6) in the actual applications become

$$L_z \left(L_y\right)^2 L_z V^{i+2} = V^i \tag{2-8}$$

$$L_z \left(L_y\right)^2 L_z V^{i+2} = L_z \left(L_y\right)^2 L_z V^i \tag{2-9}$$

to maintain the desired formal order of accuracy.

7

3. SOLUTION TO THE NONLINEAR DIFFERENCE EQUATIONS

Eq.(2-1) and its difference equation, eq.(2-6), are nonlinear, so a method of linearization is devised to reduce the equations into a soluble form. It may be advantageous to linearize the difference equations directly as shown below because the conservative-law form can be retained throughout the iterations.

Assume there exist certain relationships between the column vectors F, G, H and V, V_y, V_z, where the subscripts denote the partial derivatives.

$$dF = PAdV$$

$$dG = PBdV - PCdV_y - PDdV_z$$

$$dH = PEdV - PFdV_z - PGdV_y$$

where P, A, B, C, D, E, F and G are square matrices, PA can be interpreted as the Jacobian matrix of F with respect to V. etc. Making use of these relations, iteration formulas are obtained according to the Newton-Raphson technique.

$$V^{\ell+1} = V^\ell + \delta V$$

$$F^{\ell+1} = F^\ell + (PA)^\ell \, \delta V$$

$$G^{\ell+1} = G^\ell + (PB)^\ell \, \delta V - (PC)^\ell \, \delta V_y - (PD)^\ell \, \delta V_z$$

$$H^{\ell+1} = H^\ell + (PE)^\ell \, \delta V - (PF)^\ell \, \delta V_z - (PG)^\ell \, \delta V_y \qquad (3-1)$$

Here, ℓ indicates the iteration count. Updated functions are given on the left side of equations, while previous functions are on the right side. Since new Jacobian matrices are computed at each iteration, the convergence of eq.(3-1) is quadratic. In general, no more than five iterations are needed to ensure that δV's be less than a reasonable magnitude of tolerance ϵ. The prescribed value should be greater than the round-off error, but smaller than the truncation error due to the finite-difference approximation of eq.(2-1). A check is made to see if $|\delta V| < \epsilon$ after each iteration. If every point on a fixed j^{th} or k^{th} line satisfies the condition, this line will be dropped out from the itera-

tive process. The iterations are terminated when every line has converged solutions. This procedure is also known as the Guass-Seidel line iteration technique as the updated value is used immediately in the iteration procedure..

The correction vector δV is determined by solving a linear system of algebraic equations, which is obtained after substituting eq.(3-1) into the first equation of eq.(2-6). The system of equations has the following form

$$b_2 \delta V_2 + c_2 V_3 = d_2$$

$$a_j \delta V_{j-1} + b_j \delta V_j + c_j \delta V_{j+1} = d_j$$

$$a_J \delta V_{J-1} + b_J \delta V_J = d_J \tag{3-2}$$

with $j=3,4...J-1$. The coefficients in the first and the last equations have incorporated the boundary conditions, hence they are slightly different from the coefficients in the second equation. A general expression of these coefficients can be derived as a function of the Jacobian matrices and the mesh spacings.

$$a_j = \alpha_1 (PB)_{j-1}^{\ell} + (PC)_{j-\frac{1}{2}} / (y_j - y_{j-1})$$

$$b_j = -\frac{\Delta y_j}{2\Delta x_i} (PA)_j^{\ell} + (\alpha_2 - \beta_2)(PB)_j^{\ell} - (PC)_{j-\frac{1}{2}} / (y_i - y_{j-1})$$

$$- (PC)_{j+\frac{1}{2}} / (y_{j+1} - y_j)$$

$$c_j = -\beta_1 (PB)_{j+1}^{\ell} + (PC)_{j+\frac{1}{2}} / (y_{j+1} - y_j)$$

$$d_j = \frac{\Delta y_j}{2\Delta x_i} \left(F_j^{\ell} - F_j^i \right) + G_{j+\frac{1}{2}}^i - G_{j-\frac{1}{2}}^i + G_{j+\frac{1}{2}}^{\ell} - G_{j-\frac{1}{2}}^{\ell} \tag{3-3}$$

Note that these groups of coefficients eq.(3-3) and eq.(3-2) are used to solve for δV_j at a fixed k^{th} line. The mixed-derivatives involving values across the kth line do not enter into the expressions. A similar type of equations

and coefficients can be derived for δV_k at a fixed j^{th} line. These equations constitute a block tridiagonal system for which an efficient algorithm (described in ref.10) is readily adopted for solution. It is of interest that as $|\delta V_j| \to \varepsilon$, $|d_j|$ must approach to ε at the same rate. The recovery of the first equation eq.(2-6) at the end of iterations implies that the conservative laws are followed strictly. The weighting parameters are $\alpha_1 = 1/(1+R)$, $\alpha_2 = \alpha_1 R$, $R = \Delta Y_{j-1}/\Delta Y_j$; likewise β_1 and β_2 are obtained using $R = \Delta Y_{j+1}/\Delta Y_j$.

Substituting eq.(3-1) into the first equation of eq.(2-3) results in a block, tridiagonal system of linear equations identical to that shown in eq.(3-2). However, the coefficients differ somewhat from those given in eq.(3-3). b_j and d_j have the following relations instead.

$$b_j = -\frac{\Delta y_j}{\Delta x_i} (PA)_j^\ell + (\alpha_2 - \beta_2)(PB)_j^\ell - (PC)_{j-\frac{1}{2}}^\ell / (y_j - y_{j-1})$$

$$- (PC)_{j+\frac{1}{2}}^\ell / (y_{j+1} - y_j)$$

$$d_j = \frac{\Delta y_j}{\Delta x_i} \left(F_j^\ell - F_j^i\right) + G_{j+\frac{1}{2}}^i - G_{j-\frac{1}{2}}^i \tag{3-4}$$

Therefore the second-order accuracy in Δx can be gained in eq.(3-2) and eq.(3-3) with little extra work.

An alternate approach to linearize eq.(2-9) is to solve for $V^{\ell+1}$ directly from V^ℓ. The Newton-Raphson technique leads to relations such as

$$F^{\ell+1} = F^\ell + (PA)^\ell \left(V^{\ell+1} - V^\ell\right)$$

and the resultant coefficients closely resemble those in eq.(3-3) and (3-4), but the accuracy may not be as good because the round-off error is larger due to $|V| >> |\delta V|$. Furthermore, the derivation of coefficients at the boundaries becomes more complex (ref. 6). ($\delta V_1 = \delta V_J = 0$ will be replaced by $V_1 = V_J = V_\infty$).

4. GOVERNING EQUATIONS AND BOUNDARY CONDITIONS

The integration of the governing equations is performed along the x-axis in the y-z plane. The computational space is defined by $0 \leq y \leq H$ and $0 \leq z \leq B$, in which the plate lies on the z-axis and $0 \leq z \leq W$.

The functions in eq.(2-1)

$$F_x + G_y + H_z = 0 \qquad (2-1)$$

are defined by

$$F = \begin{bmatrix} \rho u \\ \rho u^2 + \bar{p} \\ \rho uv \\ \rho uw \\ (\rho \varepsilon + \bar{p})u \end{bmatrix} \qquad G = \begin{bmatrix} \rho v \\ \rho vu + \tau_{yx} \\ \rho v^2 + \sigma_y \\ \rho vw + \tau_{yz} \\ (\rho \varepsilon + \sigma_y)u + \tau_{yx}u + \tau_{yz}v + q_y \end{bmatrix}$$

$$H = \begin{bmatrix} \rho w \\ \rho w + \tau_{zx} \\ \rho wv + \tau_{zy} \\ \rho w^2 + \sigma_z \\ (\rho \varepsilon + \sigma_z)w + \tau_{zx}u + \tau_{zy}v + q_z \end{bmatrix} \qquad (4-1)$$

The boundary conditions are given as

$y=0$, $u = \Lambda u_y$, $v=w=0$, $e = e_w - \dfrac{2\gamma}{\gamma+1} \dfrac{\Lambda}{p_r} e_y$

         $0 \leq z \leq w$

         $w < z < h$ $u_y = w_y = e_y = p_y = \rho_y = 0$, $v=0 (\alpha=0)$, $v_y=0 (\alpha \neq 0)$

$z=0$, $u_z = v_z = e_z = p_z = \rho_z = 0$, $w=0$

$y=H$ or $u = U_\infty \cos \alpha$, $v = -U_\infty \sin \alpha$, $w=0$, $e=e_\infty$, $p=p_\infty$, $\rho=\rho_\infty$ $(4-2)$
$z=B$

-11-

where ρ, u, v, w, p and e are, respectively, the density, velocity components in (x,y,z), pressure and the internal energy. The total internal energy is $\varepsilon = e + 0.5(u^2 + v^2 + w^2)$. $\bar{p}$ indicates the pressure to be treated differently from those appearing in the stress components, which are defined as follows.

$$\tau_{yx} = -\mu u_y, \quad \tau_{yz} = \tau_{zy} = -\mu(w_y + v_z), \quad \tau_{zx} = -\mu u_z$$

$$\sigma_y = p - (\lambda + 2\mu) v_y - \lambda w_z$$

$$\sigma_z = p - (\lambda + 2\mu) w_z - \lambda v_y \tag{4-3}$$

The heat fluxes are obtained from the expressions:

$$q_y = -\frac{k}{c_v} e_y, \quad q_z = -\frac{k}{c_v} e_z \tag{4-4}$$

where

$$2\lambda + 3\mu = 0, \quad k = C_p \mu / P_r, \quad e = C_v T \text{ and } \gamma = C_p / C_v$$

μ is the viscosity coefficient given for air by

$$\mu = 2.27 \times 10^{-8} \frac{T^{3/2}}{T + 198.6} \quad \frac{lb/sec}{ft^2} \tag{4-5}$$

k is the coefficient of thermal conductivity and is related to the Prandtl number, $P_r = 0.71$ for air. C_p and C_v are the specific heats at constant pressure and volume. Their ratio, γ, is equal to 1.4 for perfect air. T denotes the temperature. α is the angle of attack.

Eq.(2-1) is supplemented by the equation of state

$$p = (\gamma - 1)\rho e \tag{4-6}$$

The boundary conditions have taken into account the slip in velocity parallel to the wall and the jump in temperature. Λ, the mean free path of air, can be estimated by

$$\Lambda = \sqrt{\frac{\pi\gamma}{2}} \frac{M}{Re} = \sqrt{\frac{\pi}{2p\rho}} \; \mu \tag{4-7}$$

Two other important parameters used very often are the Reynolds number, Re, and the viscous-inviscid interaction parameter, χ. They are defined as

$$Re_x = \frac{\rho_\infty V_\infty x}{\mu_\infty} \quad , \quad \chi_\infty = M_\infty^3 \sqrt{\frac{C}{Re_x}}$$

where M_∞ is the free-stream Mach number and C is the Chapman-Rubesin constant, $C = \mu T_\infty / \mu_\infty T$.

To facilitate the numerical computations, three new vectors are introduced as

$$V = \begin{bmatrix} \rho \\ u \\ v \\ w \\ e \end{bmatrix} \quad , \quad V_y = \begin{bmatrix} \rho_y \\ u_y \\ v_y \\ w_y \\ e_y \end{bmatrix} \quad , \quad V_z = \begin{bmatrix} \rho_z \\ u_z \\ v_z \\ w_z \\ e_z \end{bmatrix} \tag{4-8}$$

The Jacobian matrices of F, G, and H with respect to V, V_y, and V_z are

$$PA = \frac{\partial F}{\partial V}$$

$$PB = \frac{\partial G}{\partial V} \qquad\qquad PC = \frac{\partial G}{\partial V_y}$$

$$PE = \frac{\partial H}{\partial V} \qquad\qquad PF = \frac{\partial H}{\partial V_z}$$

$$P = \begin{bmatrix} 1 & 0 & 0 & 0 & 0 \\ u & \rho & 0 & 0 & 0 \\ v & 0 & \rho & 0 & 0 \\ w & 0 & 0 & \rho & 0 \\ \tfrac{1}{2}q^2 & \rho u & \rho v & \rho u & 1/g \end{bmatrix} , \quad A = \begin{bmatrix} u & \rho & 0 & 0 & 0 \\ 0 & u & 0 & 0 & 0 \\ 0 & 0 & u & 0 & 0 \\ 0 & 0 & 0 & 0 & 0 \\ que & p+g\bar{p} & 0 & 0 & g\rho u \end{bmatrix}$$

$$B = \begin{bmatrix} v & 0 & \rho & 0 & 0 \\ 0 & v & 0 & 0 & 0 \\ ge/\rho & 0 & v & 0 & g \\ 0 & 0 & 0 & v & 0 \\ gve & 0 & \gamma g\rho e & 0 & g\rho v \end{bmatrix} \quad C = \frac{1}{\rho}\begin{bmatrix} 0 & 0 & 0 & 0 & 0 \\ 0 & \mu & 0 & 0 & 0 \\ 0 & 0 & \lambda+2\mu & 0 & 0 \\ 0 & 0 & 0 & \mu & 0 \\ 0 & 0 & 0 & 0 & \gamma g u/p_r \end{bmatrix}$$

$$E = \begin{bmatrix} w & 0 & 0 & \rho & 0 \\ 0 & w & 0 & 0 & 0 \\ 0 & 0 & w & 0 & 0 \\ ge/\rho & 0 & 0 & w & g \\ gwe & 0 & 0 & \gamma g\rho e & g\rho w \end{bmatrix} \quad F = \frac{1}{\rho}\begin{bmatrix} 0 & 0 & 0 & 0 & 0 \\ 0 & \mu & 0 & 0 & 0 \\ 0 & 0 & \mu & 0 & 0 \\ 0 & 0 & 0 & \lambda+2\mu & 0 \\ 0 & 0 & 0 & 0 & \gamma g\mu/p_r \end{bmatrix}$$

and $q^2 = u^2 + v^2 + w^2$, $g = \gamma-1$, $\frac{\partial \bar{p}}{\partial \rho} = 0$, and $\frac{\partial \bar{p}}{\partial e} = 0$.

These expressions are used later in the derivation of linear system of equation and also in the analyses of stability. The Jacobians associated with mixed derivatives, i.e., $\frac{\partial G}{\partial V_z}$ and $\frac{\partial H}{\partial V_y}$, are not needed, so they are omitted from eq.(4-9).

-14-

5. MESH SYSTEM AND STABILITY ANALYSIS

The computational domain outlined in section 4 is divided into a mesh of rec-
tangular cells, each of which has variable length and height. The smallest
cell is located at the leading edge, whereas the largest cell is at the oppo-
site corner of the region. Integers are used to designate the cell number;
half-integers designate the line between two cells. This system of cells is
determined prior to the computation by means of a procedure to be described
in the following. First, an estimate is made of Δy_1 or Δy_2 using the smallest
value of the boundary-layer thickness at X=L and the mean free path of the
free stream, i.e., $\Delta y_1 = \min(\delta, \Lambda)$, where $\delta = 0.3L./\sqrt{Re}_L$ and Λ given in the
previous section. Then an exponential function is employed to determine Δy_j,
where $j=3,4...J_F$. This function relates the transformed coordinate $\bar{y}$ in
the computational space to the physical coordinate, by $y = \left(e^{c\bar{y}}-1\right)h/\left(e^c-1\right)$,
$0\leq\bar{y}\leq1$, $0\leq y\leq h$. C is the parameter to be determined iteratively in order to
satisfy the requirement that $y_1 =0.5\ \Delta y_2$, $y_{j+1} = y_j+0.5\Delta y_j$ and $y_{JF} = h$. J_F
is the number of fine cells in the y direction. On top of this system of fine
cells, there is a system of coarse cells. The height of those cells are uni-
form and obtained from $\Delta y_j = (H-h)/(JL-JF)$ with $y_{j+1} = y_j+0.5\Delta y$ and $y_{JL} = H$,
where JL is the total number of cells along the j-axis.

The width of cells is nonuniform in the region near the side edge and uniform
elsewhere. The procedure to determine Δz_k and z_k are similar to that for Δy_j
and y_j except that for this case $\Delta z_{ks} = \Delta z_{ks-1}$ are specified to insure that
fine resolution is provided at the side edge. ks designates the selected
location of the side edge. Likewise, Δx_i and x_i are estimated using the re-
quirement that $\Delta x_1 = \Lambda_\infty$, and $x_I =IL$ where IL is the total number of integration
steps.

The mesh of cells is constructed to properly resolve the gradients of flow pro-
perties that may occur near the leading edge and around the side edge. It is
unnecessary to be concerned with the efficiency and the stability of the numeri-
cal computations because as for an implicit scheme, these aspects are no longer
dictated by the CFL condition controlling Δx_i. A simple analysis of stability

is presented to show that the present algorithm indeed is unconditionally stable. Consider a set of linear equations corresponding to eq.(2-1)

$$A V_x + B V_y - C V_{yy} = 0 \qquad (5-1)$$

A, B, and C are given in section 4.

Eq.(5-1) is composed of the hyperbolic and the parabolic equations, and their difference forms obtained from the centered scheme are

$$A_j^i \left(V_j^{i+1} - V_j^i \right) = - \frac{\Delta x_i}{\Delta y_j} B_j^i \left(V_{j+1}^{i+\frac{1}{2}} - V_{j-1}^{i+\frac{1}{2}} \right) \qquad (5-2)$$

$$A_j^i \left(V_j^{i+1} - V_j^i \right) = \frac{\Delta x_i}{(\Delta y_j)^2} C_j^i \left(V_{j+1}^{i+\frac{1}{2}} - V_j^{i+\frac{1}{2}} + V_{j-1}^{i+\frac{1}{2}} \right) \qquad (5-3)$$

The amplification matrices for these equations are obtained using the Von Neumann's method (ref. 7) as

$$G_H = \frac{I - \sqrt{-1}\alpha \; A^{-1} \; B \; \sin^2 \gamma}{I + \sqrt{-1}\alpha \; A^{-1} \; B \; \sin^2 \gamma} \qquad (5-4)$$

$$G_p = \frac{I - \sqrt{-1}\beta \; A^{-1} \; C \; \sin^2 \frac{\gamma}{2}}{I + \sqrt{-1}\beta \; A^{-1} \; C \; \sin^2 \frac{\gamma}{2}} \qquad (5-5)$$

where $\alpha = \left(\frac{\Delta x_i}{2\Delta y_j} \right)^2$, $\beta = \frac{\Delta x_i}{(\Delta y_j)^2}$, $\gamma = j\Delta y_j$ and I is the unit matrix.

The eigenvectors are obtained by solving polynomials of the following equations.

$$\left| I\lambda_H - A^{-1} \; B \right| = 0$$

$$\left| I\lambda_p - A^{-1} \; C \right| = 0$$

-16-

Thus

$$\lambda_H = \left(\frac{v}{u} \, , \, \frac{v}{u} \, , \, \frac{v-c}{u} \, , \, \frac{v+c}{u} \right) \tag{5-6}$$

$$\lambda_p = \left(0, \, \frac{\mu}{\rho} \, , \, \frac{\lambda+2\mu}{\rho u} \, , \, \frac{\gamma\mu}{k\rho u} \right) \tag{5-7}$$

since they are real variables, that implies $|G_H| \leq 1$ and $|G_p| \leq 1$. Thus eqs.(5-2) and (5-3) are always stable.

If the backward scheme is used, the numerator in eqs.(5-4) and (5-5) are replaced by an identity matrix. Following the same procedure, the same conclusion is arrived at.

It is worth mentioning that numerical instability could arise if the streamwise pressure is treated on the same basis as other variables in eq.(2-1). For this case, F and A become

$$F = \begin{bmatrix} \rho\mu \\ \rho u^2 + p \\ \rho u v \\ \rho u w \\ (\rho\epsilon + p)\mu \end{bmatrix} \qquad A = \begin{bmatrix} u & \rho & 0 & 0 & 0 \\ ge/\rho & u & 0 & 0 & g \\ 0 & 0 & \mu & 0 & 0 \\ 0 & 0 & 0 & \mu & 0 \\ gue & \gamma g\rho e & 0 & 0 & g\rho\mu \end{bmatrix}$$

The corresponding eigenvalues are

$$\lambda_H = \left(\frac{v}{u} \, , \, \frac{v}{u} \, , \, \frac{uv \pm c\sqrt{u^2+v^2-a^2}}{u^2-a^2} \right) \tag{5-8}$$

$$\lambda_p = \left(0 \, , \, \frac{\lambda+2}{\rho u}, \, \lambda_3 \, , \, \lambda_4 \right) \tag{5-9}$$

They will have complex components if $u^2 + c^2 < a^2$, where a is the local sonic speed. Further, λ_3 and λ_4 in eq.(5-9) are also complex. Therefore eqs.(5-2) and (5-3) become unstable if p is used instead of $\bar{p}$. This stability problem was known in earlier work of solving the parabolic N-S equations (ref.4) and p_x was eliminated from the governing equations. A better approach is to employ

-17-

the pressure gradient obtained at the upstream station, but the improvement of accuracy is not noticeable if Δx_i's are made nonuniform (ref. 8).

The efficiency of implicit schemes is not necessarily higher than that of explicit schemes. The advantage of selecting the larger step increments and extremely fine cell sizes is penalized by a relatively large amount of computation time solving the nonlinear equations. In fact, more iterations are required in the procedure described in section 3 for regions where properties change rapidly, compared to regions near the undisturbed free stream. In general, the efficiency of a particular scheme depends upon the nature of the problem to be solved, and varies appreciably with the equation formulation and the performance of the nonlinear solver. For a leading-edge problem, ref. 4 indicates that the ADI scheme is substantially more economic to use than the straightforward explicit scheme. The present algorithm should be comparable with the ADI in the aspect of efficiency; however, there is no evidence available to verify it at this time.

6. FLOWFIELD OVER A FINITE-WIDTH PLATE

The numerical computations have focused on a case that was studied and reported in ref. 4. A limited amount of data was also available from a test facility consisting of a nozzle placed inside a Mach 12 blowdown tunnel. Due to the large drop in stagnation pressure, extremely low densities are achieved in the test section. The free stream conditions upstream of the plate have a Reynolds number, Re_∞ = 300/in and a Mach number, M_∞ = 5.15. The free stream temperature is T_∞ = 230°R, while the wall temperature is T_∞ = 460°R. The numerical results were obtained from an ADI scheme using a mesh of points with constant spacings in the transverse and lateral directions, also in the stream-wise directions. Comparisons with the experimental data were made at $\chi \cong 10$; a station displays strong merged-layer characteristics.

The computational domain and the mesh of cells were devised in a different manner than those used in ref. 4 in an attempt to properly represent the flowfield structures around the side edge. The size of the domain is given as follows: L=2 in., H=2.4 in., h=0.48 in., w=2.16 in. and b=3.03 in. The cell system is designated by the notation (JF)JLxKL(KS), as (12)32x32(20), where JL and KL are the total number of cells along y and z coordinates. The numbers in the parentheses indicate the total number of nonuniform cells along y, and the location of the side edge. The resulting cell dimensions are $\Delta y_1 = \Delta y_2 = 0.024$in., and $\Delta z_{20} = \Delta z_{19} = 0.0123$ in. A schematic of the cell system is shown in fig. 2. The streamwise increments are also nonuniform and determined by a procedure described in the previous section after assigning $\Delta x_1 = 0.024$ in. and K=30, the number of steps. Note the smallest cell used is greater than the mean free path, which is $\Lambda_\infty = 0.03$ in. for this case.

Comparisons are first made among the theoretical predictions of the pressure distributions across the stream in the lateral direction. Figure 3 shows that there are significant differences in pressure values near the side edge, but a good agreement toward the plane of symmetry and the opposite side in the free stream. The centered solution indicates a very sharp drop of pressure right at the side edge; the backward solution predicts a moderate variation,

-19-

whereas the previous ADI results display a slight change in pressure across
the side edge. It is very difficult to assess the accuracy yielded by these
computations without data from other sources. By observation from the pub-
lished results in ref. 4, the shear layer characteristics might have been par-
tially ignored because the mesh system is relatively coarse, even though the
computational domain is less than half of that used in the present computa-
tions. On the other hand, the appreciable differences between the centered
and the backward solutions are affected to some extent by the numerical dissi-
pations of the schemes. The centered scheme is known to provide more accurate
results if the solution is smooth, but may exaggerate the results for a rapidly
varying solution. Further, due to its lack of damping, small-wave length dis-
turbances tend to grow and eventually become outbound. Indeed, it was found
in the present calculation that the centered solution encountered some diffi-
culties with the iterative procedure after reaching $\chi=6.6$ at K=25 when negative
densities appeared in some cells neighboring the side edge. In contrast, the
results obtained from the dissipative backward scheme are stable throughout
the integration and appear to yield reasonable accuracy. For this reason, the
backward scheme has been employed in the entire study.

Other than the differences existing between theoretical pressure results, there
is also slight disagreements with the available experimental data in the flow
flux at the midspan of the plate. The reason for the deviation within the
boundary layer is not yet determined. The theoretical predictions of flux agree
with each other very well, except near the region where the maximum value occurs.
These curves are not asymptotic to zero at y=0, since the slip velocity is used
there.

Figure 4 presents a series of pressure distributions vs. z-coordinate. The
pressure starts out with the free stream value, slowly builds up its magnitude
as the slip velocity reduces, and finally reaches the peak value p=5.25 p_∞ at
$\chi=19.5$. At the beginning there is a smooth transition from the surface pressure
to the free stream pressure outside of the plate. It is seen in figure 4(a)
that the pressure distribution resembles closely that within a normal shock.
Figures 4(b) through 4(d) show the detailed variations of pressure as the flow
moves downstream. A discontinuity is developed within the shear layer sur-

rounding the edge, then dissipates and diffuses sideways as the shear layer grows thicker and reduces the magnitude of gradients. At the end of the computation, X=5.35 or X=2 in., the side edge has started to lose its influence on the local flowfield. The mechanism producing the pressure discontinuities must originate from the strong interactions between the flow and the plate. Due to the presence of a plate in the flow, the kinetic energy transforms directly into the internal energy on top of the plate. This process does not take place immediately because the rarefaction effect predominates at the leading edge. The flow over the plate adjusts itself rather quickly, but slowly in the shear layer around the edge. Therefore, the pressure retains a higher value for a longer distance outside the plate until the physical dissipation finally smooths out the nozzles. Unfortunately, no experimental data are available in this region, so confirmation of the prediction cannot be made at this time. Note that the side edge effect has almost reached the center-line as indicated in figure 4(e). This points out the possibility that the flow cannot be considered two-dimensional at X=L when the aspect ratio, W/L, is less than unity.

The distributions of the coefficients of skin friction, $\tau_{xy}/\frac{1}{2}\rho U_\infty^2$, and of heat transfer, $(q+u\tau_{xy})/\rho_\infty U_\infty(H_{t_\infty}-H_{t_w})$, are given in figures 5(a) and 5(b), respectively. As explained earlier, the shear layer increases its extent with decreasing values of χ, and moreover the shear layer creates relatively higher heating at the edge compared to that at the center. Judging from these figures, however, the flow field remains two-dimensional at the centerline.

Figure 6 shows the velocity vector, constant contours of w, pressure, and temperature plotted on the plane normal to the x-coordinate at χ=5.35. It indicates an upward motion of flow above the plate. Near the edge, however, a sideways motion predominates. Away from the side region, there are no transverse and lateral velocity components. The lateral velocity is plotted in constant contours to show that the highest value occurs somewhere out in the free stream and that w changes rapidly at the side edge. The pressure contours exhibit a leading-edge oblique shock above and a side-edge shock next to the side edge. The temperature contours disclose the location of a distontinuity near the edge, which has a stronger intensity than the leading-edge shock.

More computations were carried out at angles of attack, $\alpha=10^O$ and -10°, which represent the wind and the lee sides of the plate, respectively. The primary purpose is to check the capability of the numerical algorithms under more severe conditions. It would be of interest from the practical point of view to consider the entire flowfield on both sides of the plate, but this necessitates extensive modification of the program while it adds little value to our objective. In the present approach, these two cases are treated independently, with different boundary conditions imposed at $y=0$ and $b \leq z < w$ to approximate the flow vector continuation. Other than this modification, free stream velocity becomes $u_\infty = U_\infty \cos\alpha$ and $v_\infty = -U_\infty \sin\alpha$. The computational region and the cell system are the same as those for $\alpha=0^O$. Despite the fact that this approach sacrifices physical velocity, the predictive potential of the algorithm can still be evaluated and assessed.

Figure 7 shows the pressure distributions vs. z-coordinate given at selected x-stations. The wiggles in pressure distributions are believed to be caused by insufficient space resolution, since flow properties change more drastically around the side edge. Regardless of the local numerical problems, the computation was completed at $x=2"$ for both cases. The x-component of shear stress and the heat fluxes behave in the same manner as those predicted for $\alpha=0^O$, hence they are not repeated. One additional feature, which bears no counterpart in the $\alpha=0^O$ case, is the flow separation across the lee side of the plate and a stronger lateral flow on the wind side. Shown in fig. 8 are the skin friction coefficients, $\tau_{yz}/\frac{1}{2}\rho U_\infty^2$, vs. z on both sides of the plate. The influence of the side edge is felt at an earlier station on the center plane. It is indicative that for a plate of aspect ratio equal to unity, the flow on the plane of symmetry is definitely not two-dimensional when the plate is placed at an angle to the free stream. The significance of the results obtained is in the discovery of separated flow immediately over the side edge. The lateral extent of separation is seen to be proportional to the streamwise coordinate. The separation becomes stronger as x increases. Figure 9 shows that the transverse extent of the cross flow separation also increases with x.

Figure 10(a) shows the lee side cross flow velocity vector obtained at x=2" and 4". It exhibits a stronger lateral reversed flow region farther away from the leading edge. But, a complete vortex has not yet been established, probably due to the small angle of attack, which is not able to produce a full vortex. Figure 10(b) is the constant contour plots of lee side pressure at two stations. The pressure discontinuity adjacent to the side grows as does the lateral velocity.

All the computations were performed on an IBM 370-168 computer using approximately four minutes of CPU. The computation time required can vary from one case to another, because even with the same number of cells and streamwise steps, some may need more iterations in solving the nonlinear difference equations than others. An understanding of flow characteristics is helpful in the selection of computational region and mesh, which could reduce the requirement of computation time and increase the accuracy of the results.

7. CONCLUSIONS

It has been shown that the finite-difference methods constructed using the method of fractional steps has promising potential in solving the parabolic Navier-Stokes equations. This study has concentrated on the computation of viscous flow passing a finite-width plate, and utilized both centered and backward difference schemes to integrate the equations along the streamwise coordinate. The applicability of the centered scheme is found to be susceptible to shocks and shear layers in the flow field and hence not used in calculations. The solutions obtained from the backward scheme appear to be stable and reasonably accurate. The numerical algorithm is featured with the conservative-law formulation in the difference equations and with a linearization procedure that is also consistent with the conservative law. Remarks pertaining to the flat-plate problem at flow incidence are summarized as follows:

1. This work has revealed the existence of a shear layer around the side edge of the plate. Its intensity reduces from the peak value near the leading edge as the flow moves downstream, but it remains discernable well into the weak-interaction regime.

2. The pressure distribution along the center line is more sensitive than other measurable quantities to the flow expansion about the edge. For the conditions used, the flow should be treated three-dimensionally when the aspect ratio, W/L, is close to unity.

3. A cross flow separation is predicted on the lee side at $\alpha=-10^{o}$; however, the complete formation of a vortex has not been established.

4. The solution to this problem can be obtained from the elliptical Navier-Stokes equations using a time-dependent method, but it would require 100 times as much computation time.

5. The present method of solution is restricted to a class of viscous flow problems which do not involve a local reversed flow region in the direction of the main stream and the streamwise pressure gradient is negligible.

-24-

REFERENCES

1. Patankar, S. V., and Spalding, D. B., Int. J. Heat Mass Transfer, 15, pp. 1787-1806, 1972.

2. Briley, W. R., J. Comp. Phys., 14, pp. 8-28, 1974.

3. Rubin, S. G., and Lin, T. C., J. Comp. Phys., 9, pp. 339-364, 1972.

4. Nardo, C. T., and Cresci, R. J., J. Comp. Phys., 8, pp. 268-284, 1971.

5. Yanenko, N. N., The Method of Fractional Steps, Springer-Verlag, Berlin-Heidelberg, 1975.

6. Cheng, S. I., A Critical Review of Numerical Solution of Navier-Stokes Equations in Progress in Numerical Fluid Dynamics, edited by H. J. Wirz, Springer-Verlag, Berlin-Heidelberg, 1975.

7. Richtmeyer, R. D. and Morton, K. W., Difference Methods for Initial-Value Problems, second ed., Intersicence Publishers, New York, 1967.

8. Li, C. P., Viscous Flowfield Solutions on a Sharp Plate (to be published).

9. Douglas, J. and Rachford, H. H., Trans. Amerc., Math, Soc., 82, pp. 421-435, 1956.

10. Isaacson, E. and Keller, H. B., Analysis of Numerical Methods, John Wiley & Sons, New York, 1966.

LIST OF FIGURES

J + 1 k − 1	J + 1 k	J + 1 k + 1
J k − 1	J + 3/2 k J k	J k + 1
J − 1 k − 1	J + 1/2 k J − 1 k	J − 1 k + 1

J − 1/2 k

Figure 1.— Notation of cell system.
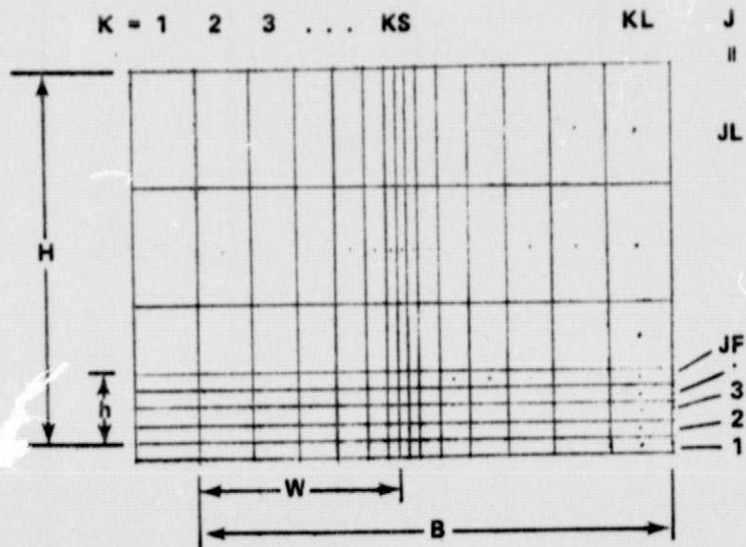
(b) CELL SYSTEM

FIGURE 2
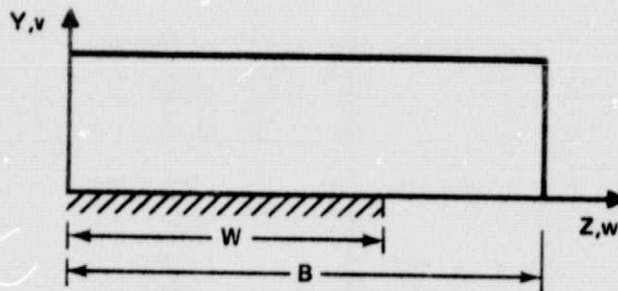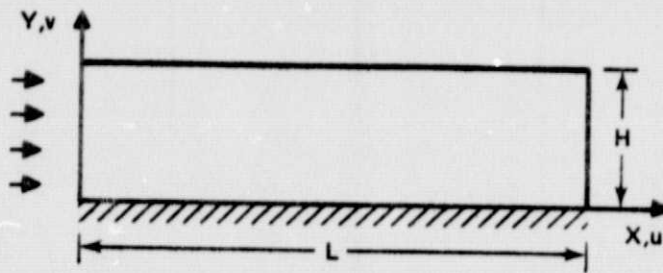
(a) COORDINATE SYSTEM

Figure 2.— Schematic of the coordinate system.
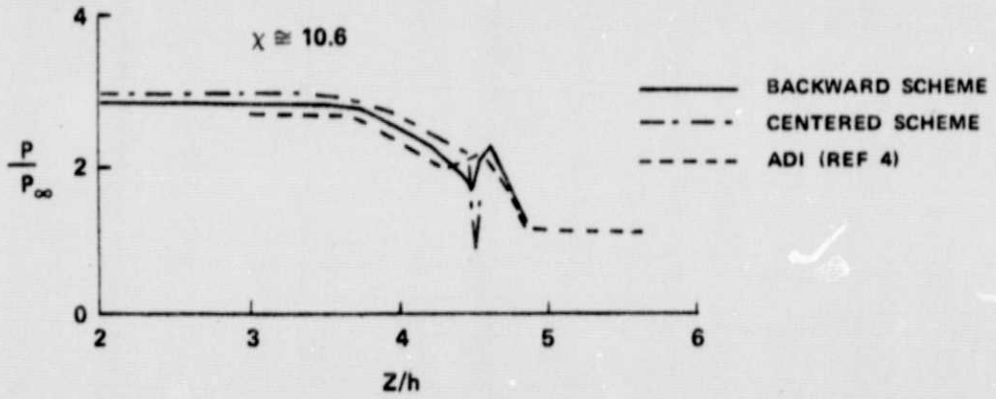
(a)
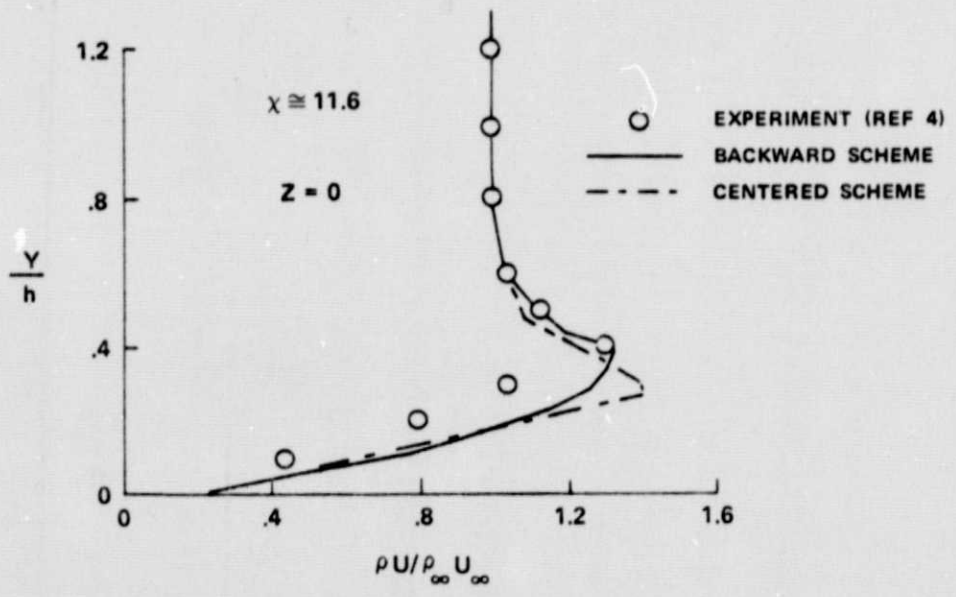
(b)

FIGURE 3
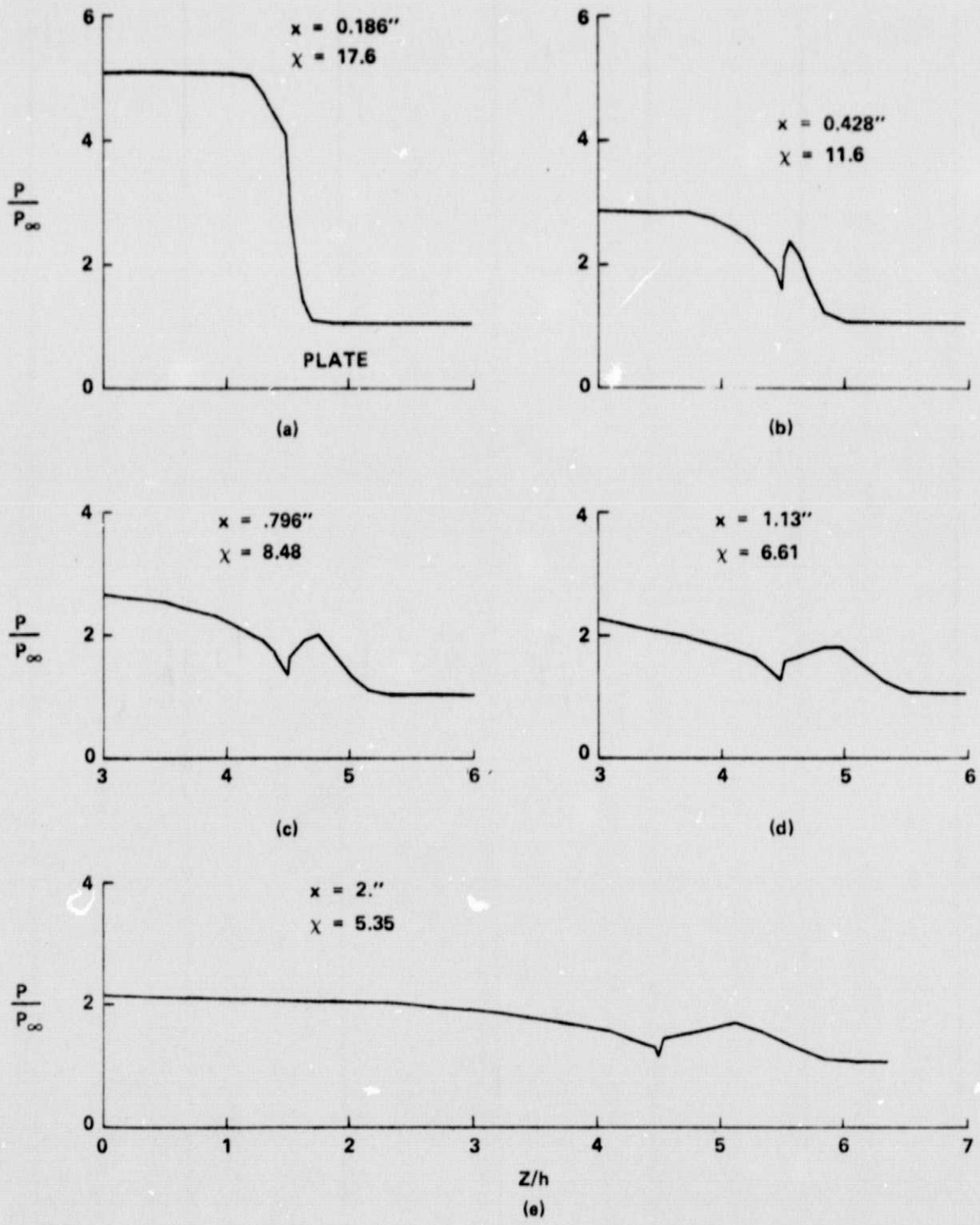
FIGURE 4

FIGURE 5

-33-

(a)

(b)

FIGURE 6

-34-
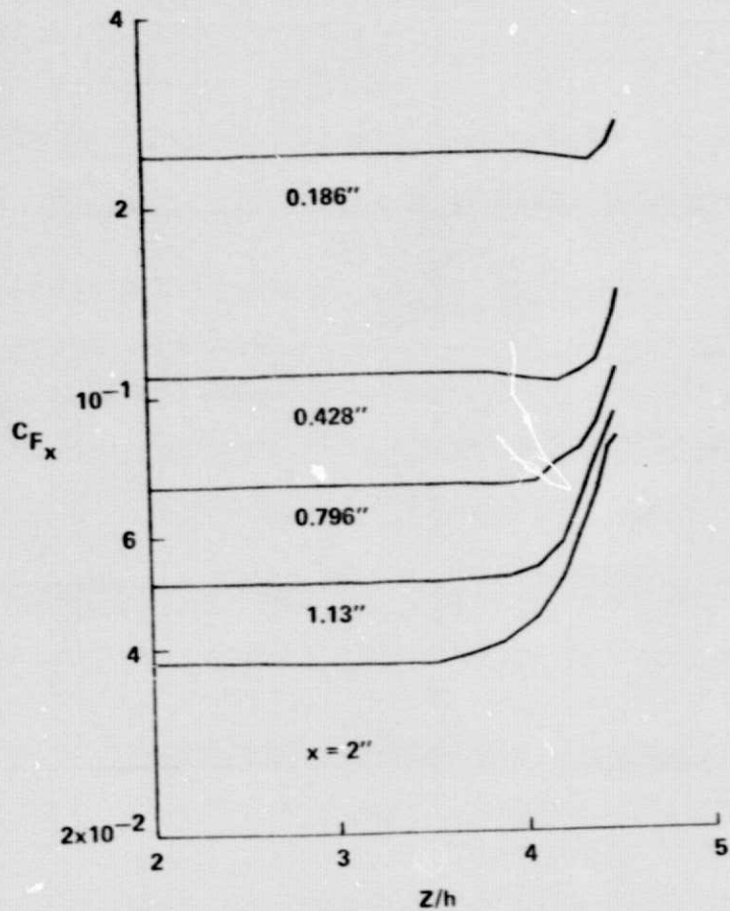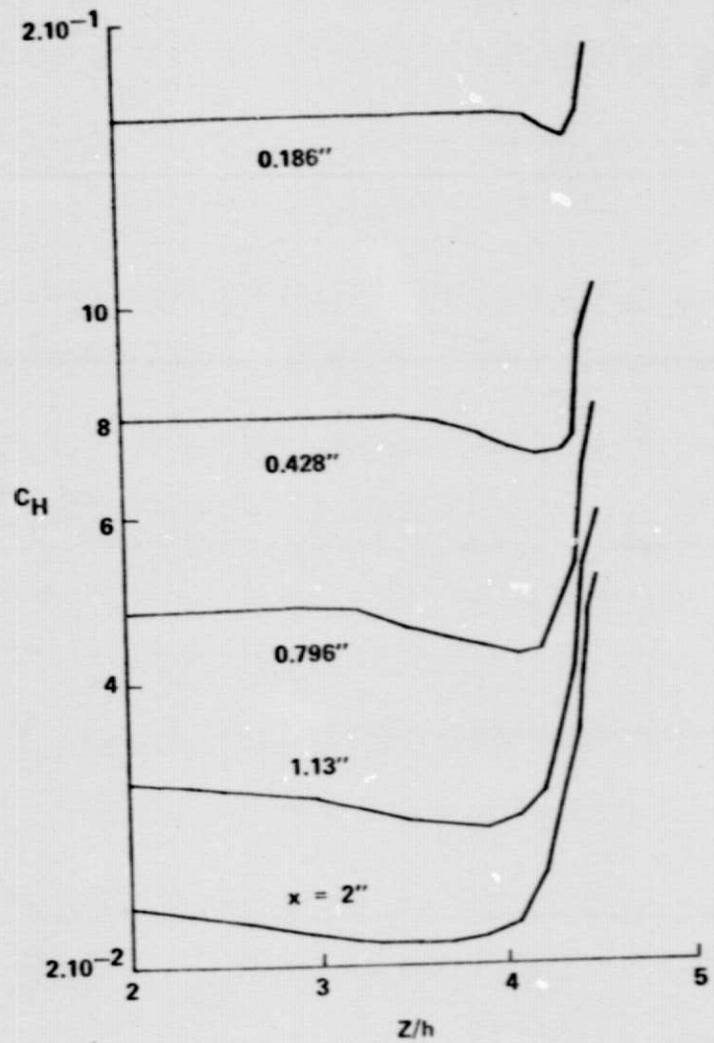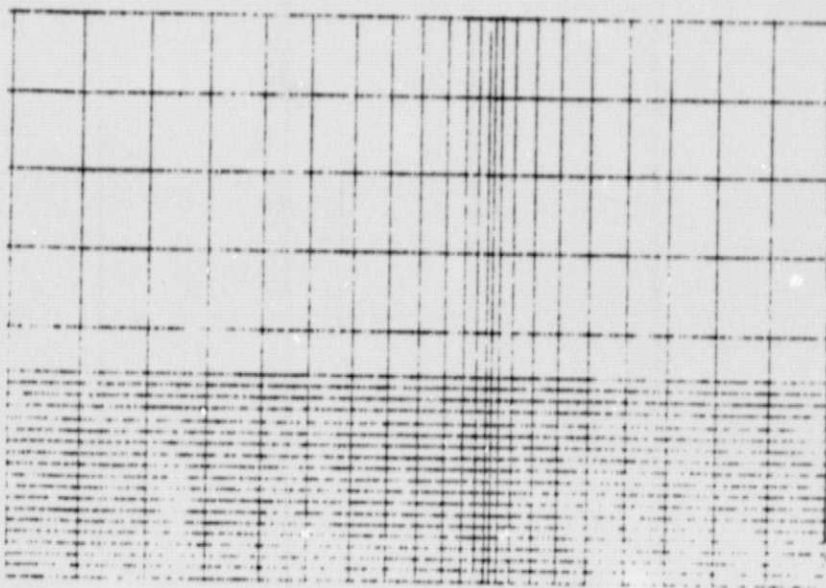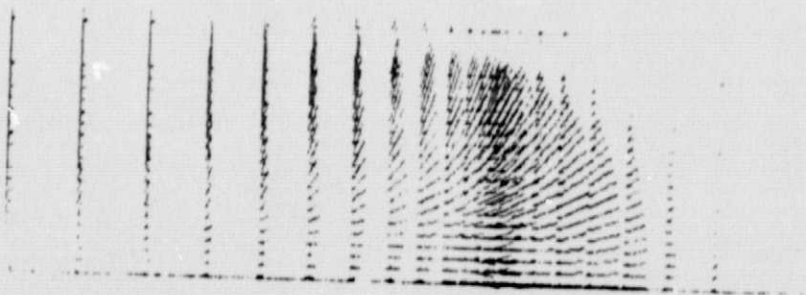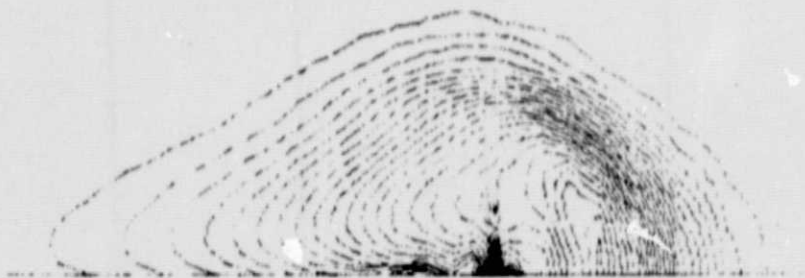
(c)
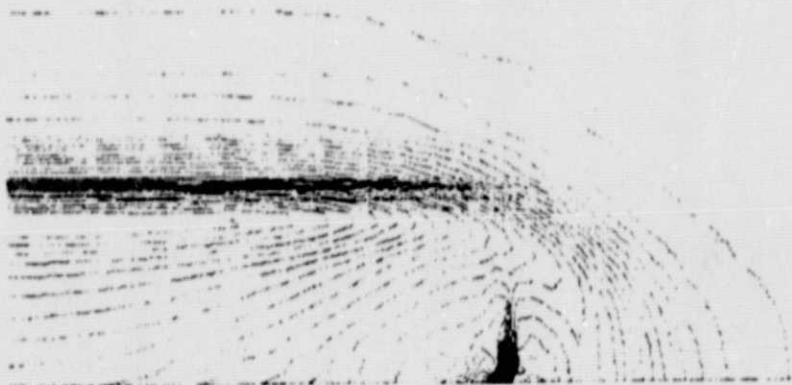
(d)
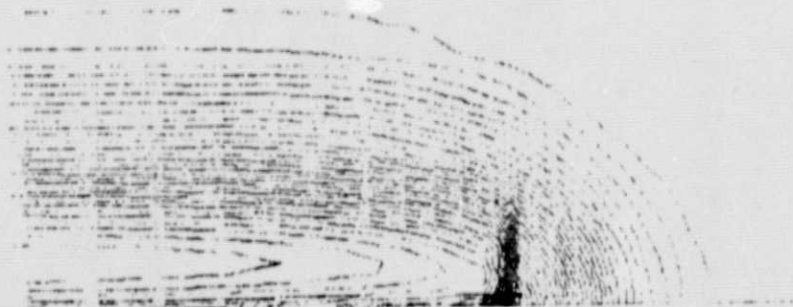
(e)

FIGURE 6

SAME CONDITIONS & MESH CELLS, $a = 10°$ AND $-10°$
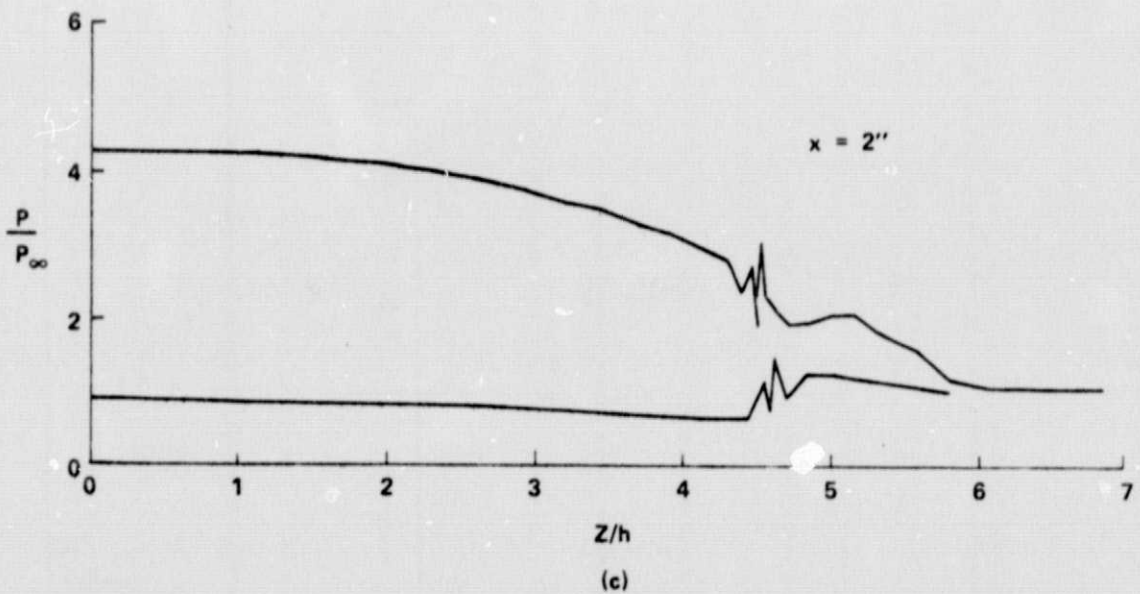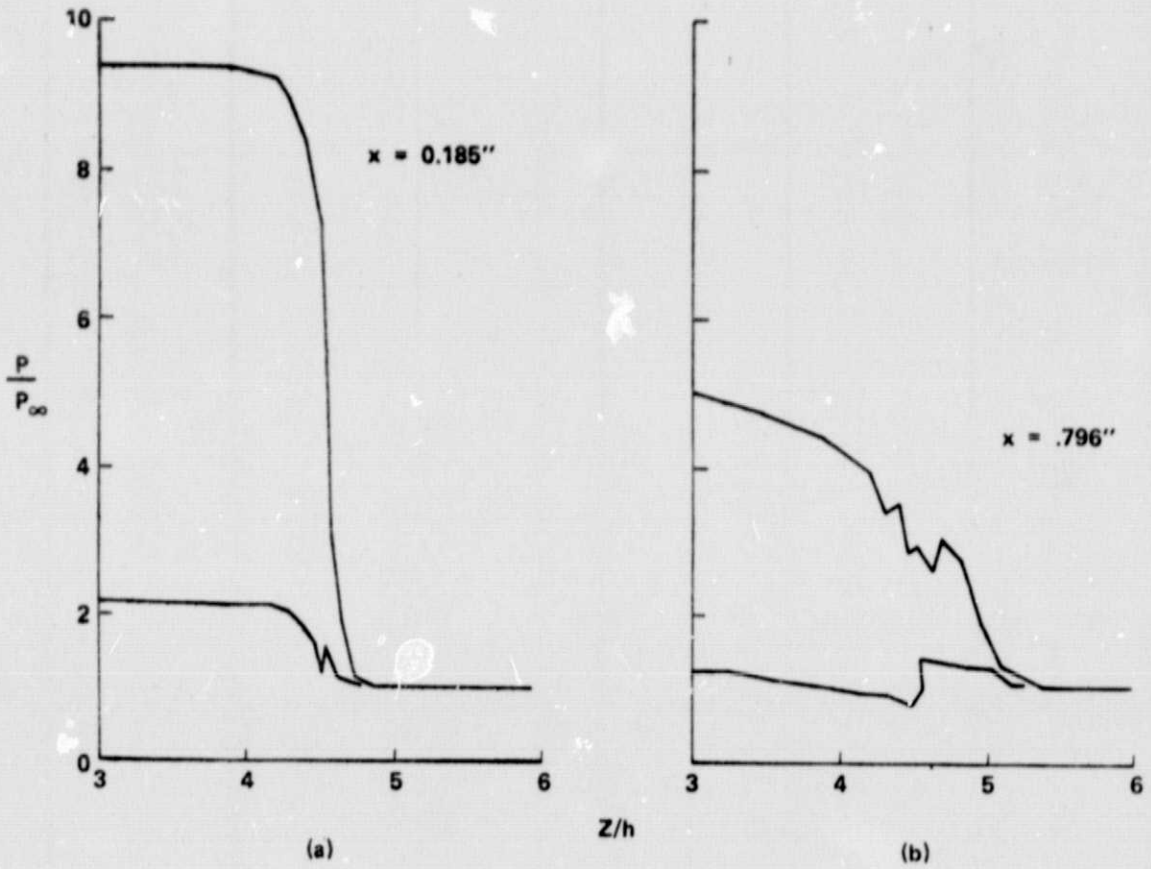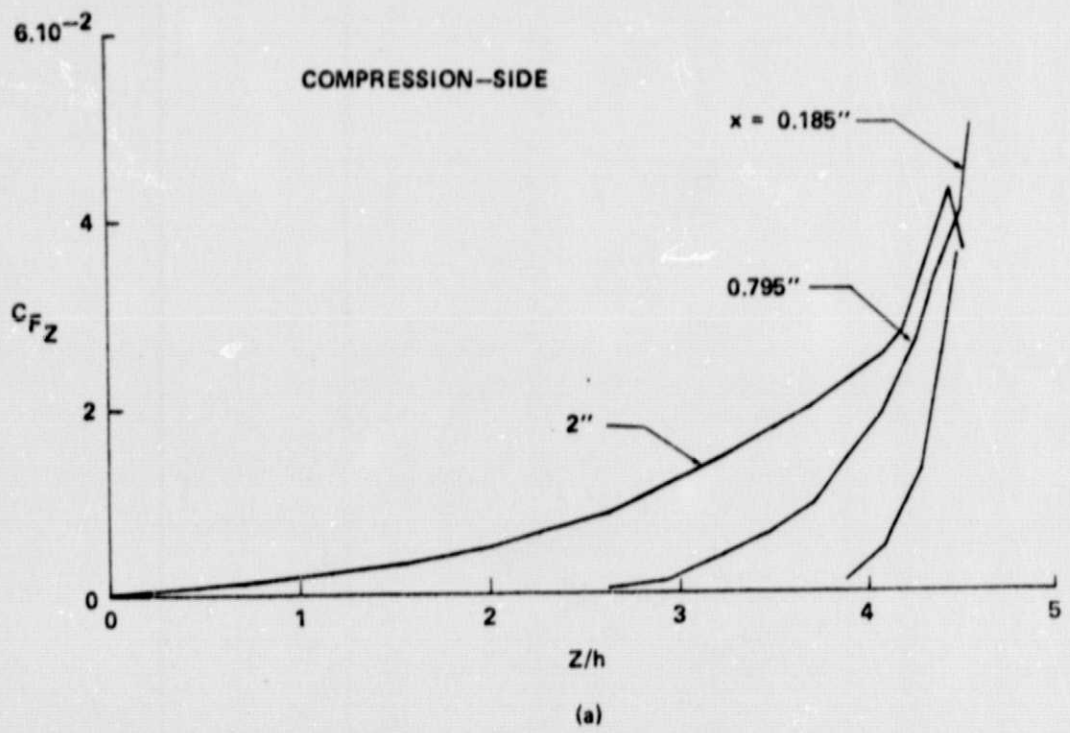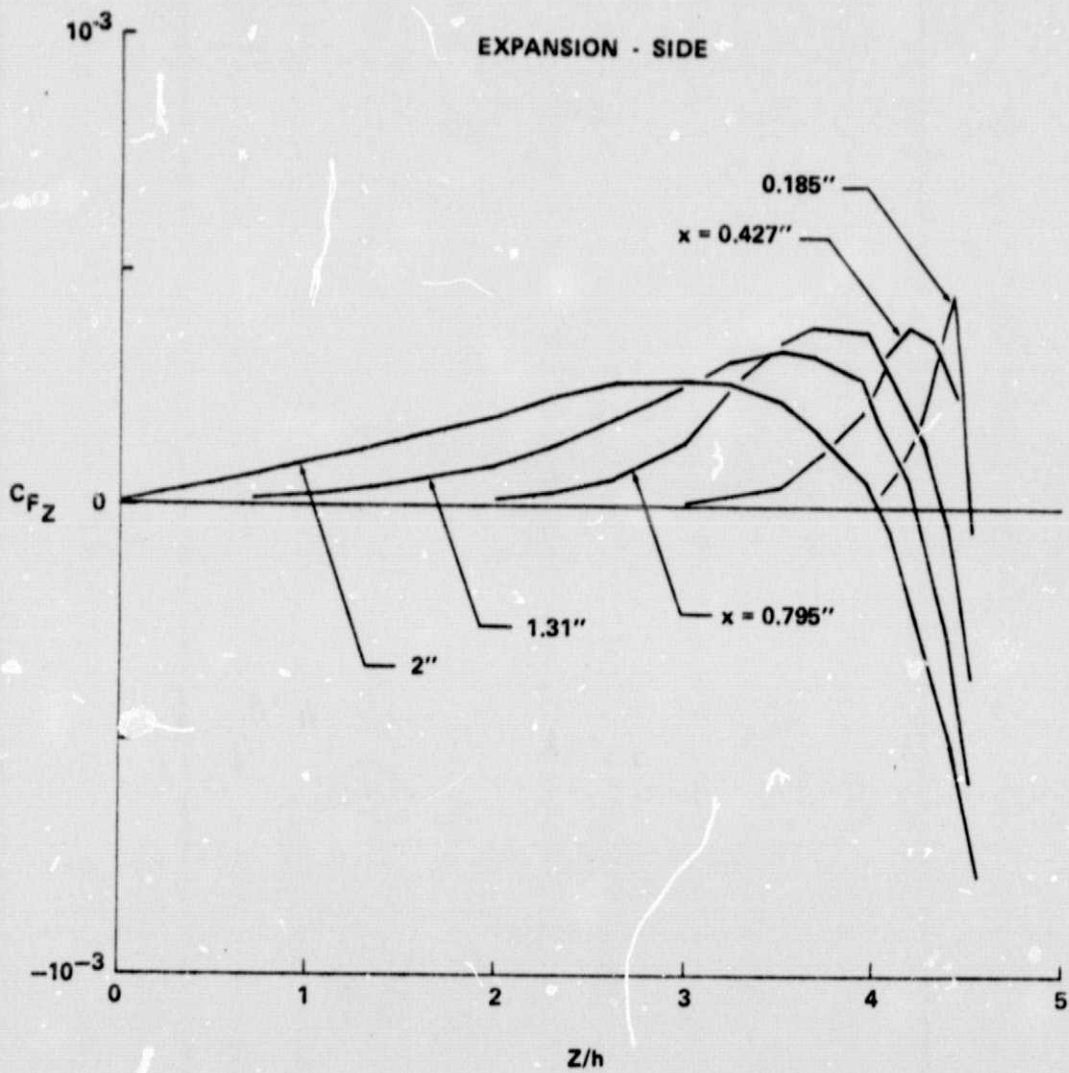
(a)

(b)

(c)

FIGURE 7

COMPRESSION–SIDE

6.10^{-2}

$x = 0.185''$

0.795''

2''

C_{F_Z}

4

2

0

0   1   2   3   4   5

Z/h

(a)

FIGURE 8

EXPANSION - SIDE

0.185″

x = 0.427″

c_{F_Z} 0

2″

1.31″

x = 0.795″

10^{-3}

-10^{-3}

Z/h

(b)

FIGURE 8

-38-
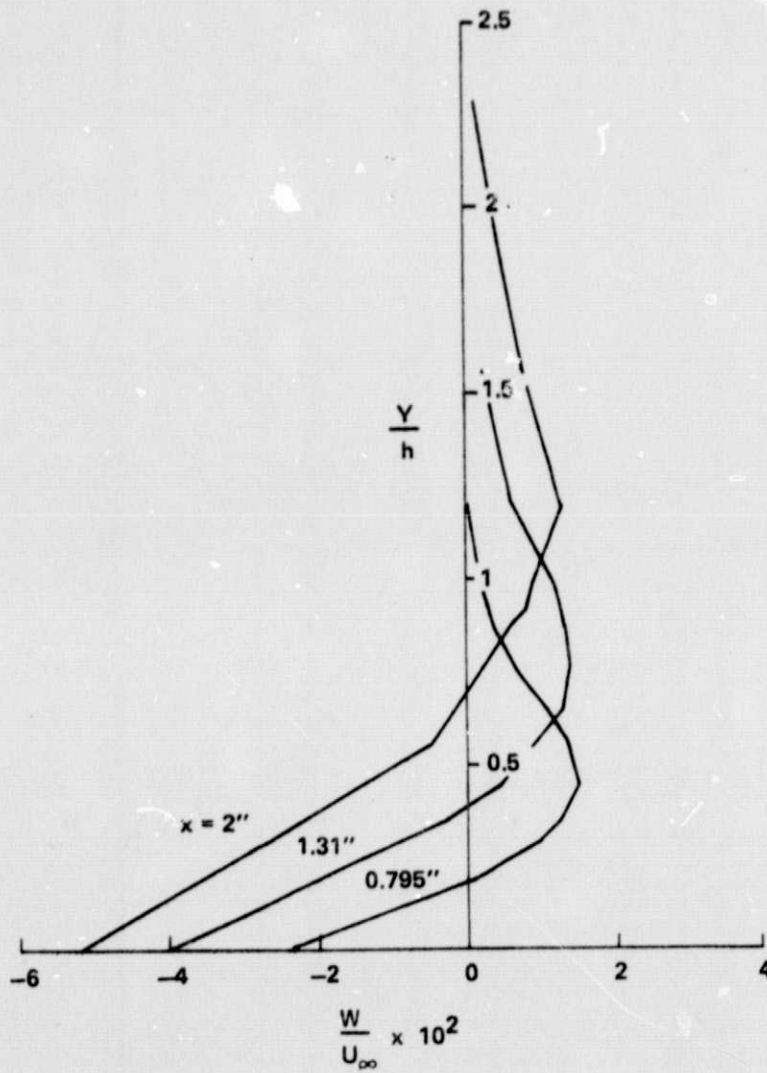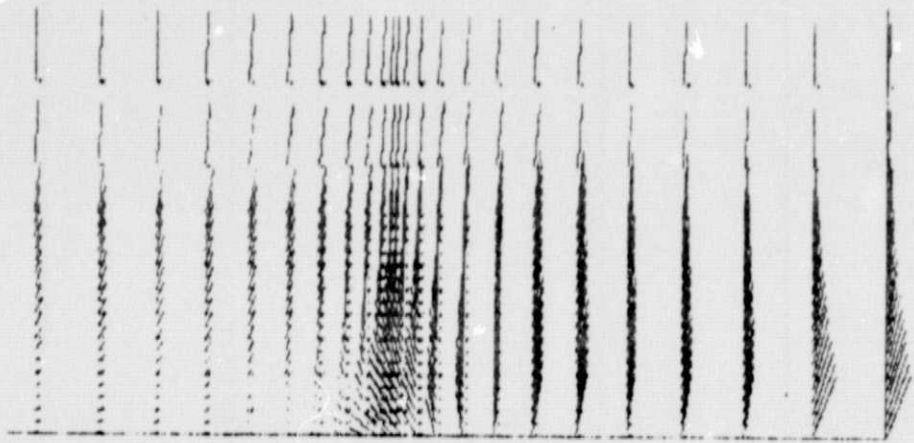
FIGURE 9

2 INCHES

(a)
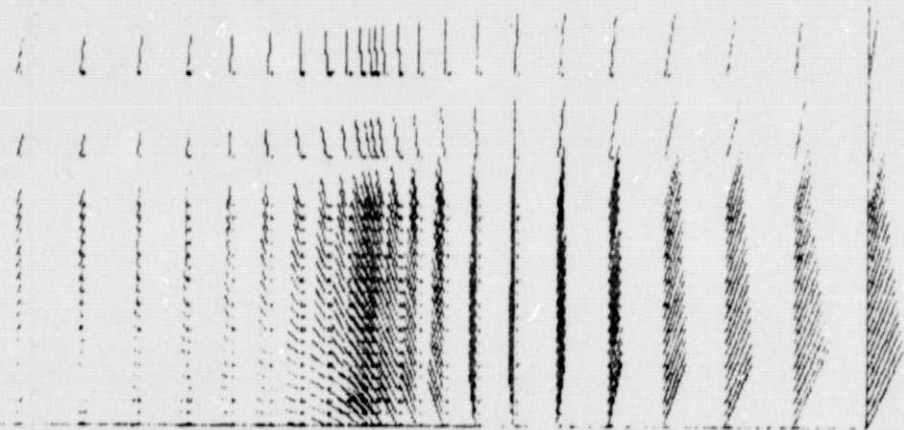
4 INCHES
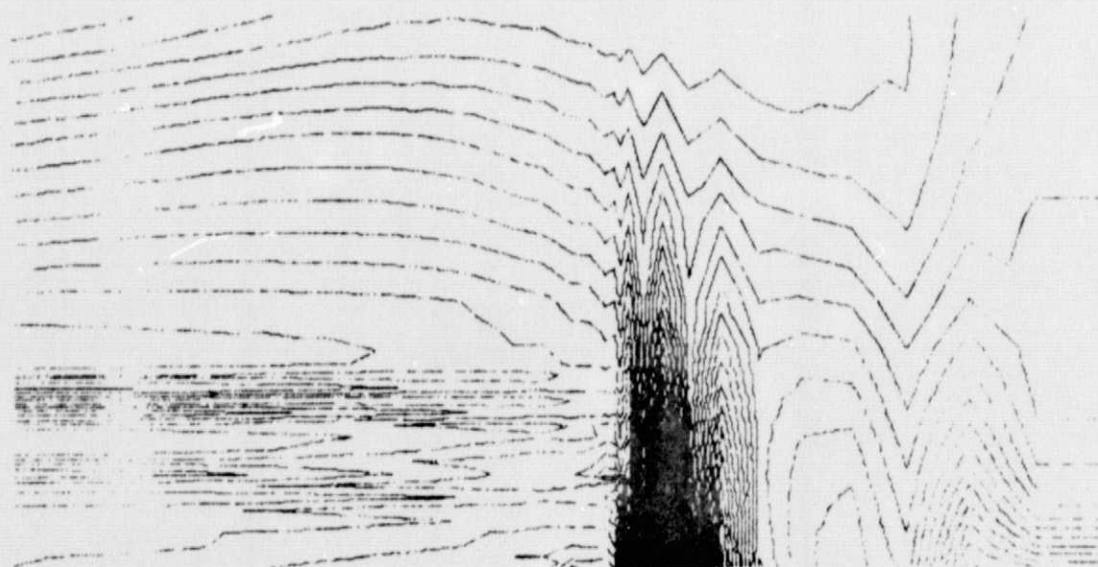
(b)

FIGURE 10
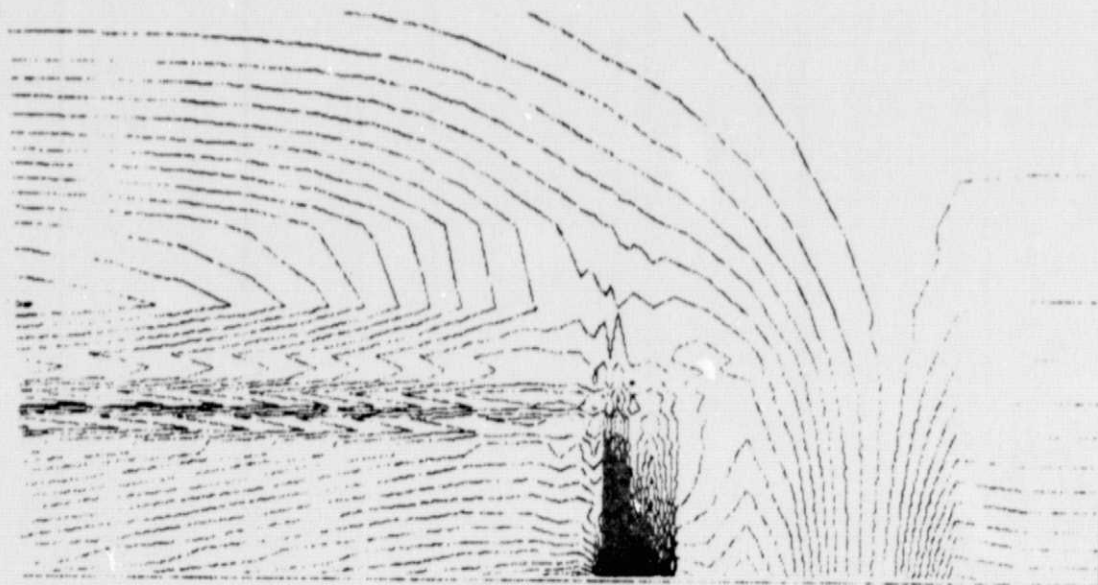
2 INCHS

(c)

4 INCHES

(d)

FIGURE 10